Rational modulation of p-n homojunction in P-doped g-C$_3$N$_4$ decorated with Ti$_3$C$_2$ for photocatalytic overall water splitting

Zizheng Ai[a], Yongliang Shao[a], Bin Chang[a], Lei Zhang[a], Jianxing Shen[b], Yongzhong Wu[a], Baibiao Huang[a], Xiaopeng Hao[a],*

[a] State Key Lab of Crystal Materials, Shandong University, Jinan 250100, PR China
[b] Department of Materials Science and Engineering, Qilu University of Technology, Jinan, 250100, PR China

ARTICLE INFO

ABSTRACT

As a metal-free polymeric semiconductor, graphitic carbon nitride (g-C$_3$N$_4$) is a promising candidate for photocatalytic water splitting but suffers from the insufficient optical absorption and sluggish utilization of photocarriers. Herein, based on the energy band engineering theory, a new design philosophy of tunable p-n homojunction is proposed and realized in a novel P-doped g-C$_3$N$_4$ (PCN) material. Through regulating the tendency of transformation in p-n homojunction, a strong internal electric field is built and integrated with two secondary internal electric fields by further decorating with Ti$_3$C$_2$, leading to the formation of a triple-internal electric field system. Thus the spatial separation efficiency of photocarriers is improved and their lifetime is prolonged. The specific photocatalyst exhibits excellent overall water splitting performance in pure water with a notable quantum yield. This work presents a peculiar concept of adjustable p-n homojunction and holds great significance for the rational design of advanced photocatalyst in water splitting.

1. Introduction

As a clean, inexhaustible energy, the solar energy is regarded as the most potential and eco-friendly choices of producing renewable fuels for sustainable environment and energy development [1–3]. In order to achieve this aim, water splitting into H$_2$ and O$_2$ via photocatalytic system is a scalable approach for solar-chemical conversion [4–7]. Although tremendous efforts have been made during the past decades, the photocatalytic system for overall water splitting still encounters several challenges. Firstly, the high Gibbs free energy of 237 kJ/mol requires to be overcome [8]. Secondly, the O$_2$ evolution of four-electrons process needs large thermodynamic function [9]. Thirdly, the separation efficiency and transfer ability of charge carriers should match well with redox-active sites. Finally, abundance, cheapness and robustness are important reference criterions of photocatalysts for practical application. Therefore, developing novel materials and designing new photocatalytic systems for overall water splitting have a long way in this field [10–13].

Graphitic carbon nitride (g-C$_3$N$_4$) has recently attracted intensive focuses on account of its robust two-dimensional (2D) structure, earth-abundance, chemical modification and suitable thermodynamic potentials for overall water splitting [14–17]. However, pure g-C$_3$N$_4$ suffers from lots of deficiencies such as fast recombination of photocarriers, low solar-energy utilization and insufficient active sites [18–20], which seriously restrict its application. Thus, various techniques and modification methods such as constructing compound system with other materials, modulating conditions and adjusting morphologies have been applied to strengthen solar water splitting activity [21–23]. Recently, for g-C$_3$N$_4$ elemental doping is a hot topic in modifying its band structure and creating more active sites [24,25]. Whereas, deep exploring the relationship between semiconductor type transformation and doping regulation is rarely involved. What's more, the repeating tri-s-triazine units and π-π conjugated electronic system of g-C$_3$N$_4$ are the root causes of fast charges recombination. Based on this reason, designing a p-n junction via incorporating other material with g-C$_3$N$_4$ is an essential approach to enhance its photocatalytic performance, in which a strong internal electric field is formed at the interface due to the large differences in work functions and potentials. Then combining the equilibration of Fermi-level, the photogenerated electron-hole pairs are separated efficiently and transfer to redox-active sites quickly [26–28]. However, the difficulty in energy band matching, structural and interfacial compatibility between two different semiconductors hinders the further improvement of its photocatalytic performances. Conversely, p-n homojunction, existing in one material,

---

exhibits potential merits of good compatibility, strong interaction, flexible handling and feasibility [29], which can provide a successive band bending for rapid charge separation and transfer through the interface. At present, relevant studies about p-n homojunction are mainly concentrated in inorganic materials, such as GaN [30], ZnO [31], TiO_2 [32] and α/β Ga_2O_3 [33]. As a traditional n-type semiconductor, g-C_3N_4 has been little studied in the transformation of p-n homojunction [34]. Therefore, constructing and regulating p-n homojunction in g-C_3N_4 will be the key precondition to establish the internal electric field, the effect of which will be further magnified by means of imbedding an unique mediator into p-n homojunction to build two little internal electric fields.

Transition metal carbide (MXene) Ti_3C_2, prepared by etching away "A" layers from MAX phases, shows outstanding prospects in energy field [35–38]. The excellent conductivity endows it with an ideal mediator in p-n homojunction, generating two little built-in internal electric fields naturally [39,40]. In the meanwhile, the specific layered structure of Ti_3C_2 can effectively insulate the photo-generated electrons from holes. Besides, water can fully infiltrate the interlayers of Ti_3C_2 with rich hydrophilic functionalities [41]. Furthermore, tremendous functional groups originating from the etching reaction also provide numerous redox active sites for water splitting into H_2 and O_2 [42]. Based on above analysis, it is significant to design a g-C_3N_4 material with adjustable p-n homojunction decorated with Ti_3C_2, which can greatly prolong the lifetime of separated electron-hole pairs and make them arrive the redox active sites for overall water splitting.

In this work, in order to manipulate the spatial motion of photo-carriers effectively, an original conceptual design of tunable p-n homojunction is presented on the basis of the energy band engineering theory. And this specific design idea is implemented in a novel P-doped g-C_3N_4 (PCN) material for the first time. The strong internal electric field existing in p-n homojunction is well integrated with the two secondary internal electric fields through further decorating with Ti_3C_2, which synergistically improves the efficiency of charge carrier separation and transportation via the triple-internal electric field. This unique photocatalytic system displays a glorious overall water splitting ability and good stability. Our synthetic strategy offers a new perspective of developing novel and efficient photocatalysts through regulating p-n homojunction as a potential candidate for effective solar energy conversion.

2. Design concept

Under the guidance of energy band engineering theory, a novel concept of tunable p-n homojunction has been designed in PCN via regulating the doping level of P element. As shown in Scheme 1, the concentration difference of charges at the interface results in the re-distributing and a new equilibrium of E_f level is obtained, building a powerful unidirectional electric field. Therefore, the photo-generated electrons (p-type part) transfer to n-type part with the low CB edge and the photo-generated holes (n-type part) move towards p-type part with the high VB edge. Furthermore, Ti_3C_2 acts as a mediator relying on its unique layered structure. New little internal electric fields are formed between Ti_3C_2 and n-type part or p-type part in the p-n homojunction, which promote photogenerated holes (electrons) move to Ti_3C_2 as well as prevents the transfer of electrons (holes). Finally, the high efficiency of charge transfer and separation is realized with the help of this triple-internal electric field in the p-n homojunction decorated with Ti_3C_2.

3. Results and discussion

The typical preparation process of phosphorus doped g-C_3N_4/Ti_3C_2 (PCNT-3-5) is illustrated in Fig. S1. A novel inverse phosphatization technique is firstly designed to regulate the phosphatizing level of CN. The evaporation of ethanol hastens the drying process of CN in which many cracks are gradually formed due to the non-homogeneous stress rupture (Fig. S2). And through these cracks, PH_3 enters into CN easily and achieves a better phosphating effect as well as products avoid to be contaminated by phosphate sources. The morphology of samples was analyzed by scanning electron microscopy (SEM). As shown in Fig. 1a, the pristine CN is distorted and wrinkled. After the phosphating treatment, PCN-3 features a novel macro-porous nanosheet structure (Fig. 1b), which gives itself a larger specific area and many active sites deriving from the structure defects. It can be seen that Ti_3C_2 (Fig. S3) is uniformly distributed across the PCN-3, which provides additional active sites as well as links the broken PCN sheets (Fig. 1c). N_2 adsorption-desorption isotherms also confirm that Ti_3C_2 makes a great contribution to the improvement of specific surface area (Fig. S4). Furthermore, it is observed that Ti_3C_2 is embedded into PCN and maintains good layered structure (Fig. 1c, inset). Finally, the compound photocatalyst PCNT-3-5 was successfully prepared. In order to study the phosphatizing level of CN, a series of phosphating experiments were conducted at different temperatures. Table S1 shows that the weight percent of P increases with the increasing of temperature at first and then remains constant, which reveals that the phosphatizing process achieves a thermo-dynamic equilibrium. SEM images (Fig. S5) show that PCN-3 possesses the optimal macro-porous structure. The crystallinity of samples gets better during the phosphatizing process and PCN-3 displays the best at 400 °C (Fig. S6). It is confirmed that Ti_3C_2 combines well with PCN-3 and its structure avoids to be broken with appropriate doping ratio (Fig. S7). Besides, as shown in Fig. S8a, Ti_3C_2 can't be combined with PCN-3 well via a simple mechanical grinding experiment. High resolution transmission electron microscope (HRTEM) was conducted to further investigate the distinct morphological change and crystallinity tendency. Ti_3C_2 has a flexible structure with an obvious characteristic lattice spacing of 0.96 nm (Fig. S8b). As shown in Fig. 1d, CN sheets pile one atop another and stagger together. In addition, the disordered basal plane domain means that the raw CN has poor crystallinity (Fig. S9). After phosphating, numerous macro-pores are distributed uniformly on the surface of PCN-3 (Fig. 1e). The emerging porous feature provides a better area for assembling active sites, which can enhance the separation of reagents and products through the porous structure as well as utilize light adequately. Besides, the characteristic lattice fringe of 0.325 nm being assigned to the (002) plane of CN appears randomly in Fig. S10, which indicates that the crystallinity is modified at the local region of CN via doping of P element. The well combination of Ti_3C_2 and PCN-3 can be observed in Fig. 1f. The clear distribution of Ti_3C_2 guarantees its strong embedded ability and tight interaction with PCN-3. Meanwhile, the corresponding energy dispersive spectrometry (EDS) mapping images of PCNT-3-5 demonstrate the presence and homo-geneous distribution of C, N, P and Ti throughout the composite material (Fig. 1g).

The crystal structure of the as-obtained samples was evaluated by X-ray diffraction (XRD). As shown in Fig. 2a, the main characteristic diffraction peak of (002) at around 27.5° is observed clearly in all diffraction spectra, which originates from the typical interlayer stacking peal of CN. Another peak of (100) at 13.1° is relatively weak and negligible due to the smaller planar size or the heptazine units [43]. In addition, PCNT-3-5 also displays the typical diffraction peaks of Ti_3C_2 (Fig. S11). Meantime, the peak intensity of Ti_3C_2 is more obvious with increasing doping ratios (Fig. S12). Compared with the peak of (002) in CN, both PCN-3 and PCNT-3-5 exhibit a right shift at about 27.5° (Fig. 2a, inset), indicating a decrescent interlayer spacing. Similar results can be found from the PCN samples prepared at different phos-phatizing temperatures (Fig. S6). The above phenomena stem from the successful doping of P element, resulting from its larger atomic radius than C element [44]. The Fourier transform infrared spectroscopy (FTIR) spectra were conducted to study the structural variation after doping P element. As described in Fig. S13, the representative stretching modes at the range of 1200-1600 cm^{-1} are relevant to carbon-nitrogen (CN) heterocycles [45], which can be noticed both in CN and PCN-3 samples. The breathing modes of tri-s-triazine (C_6N_7-
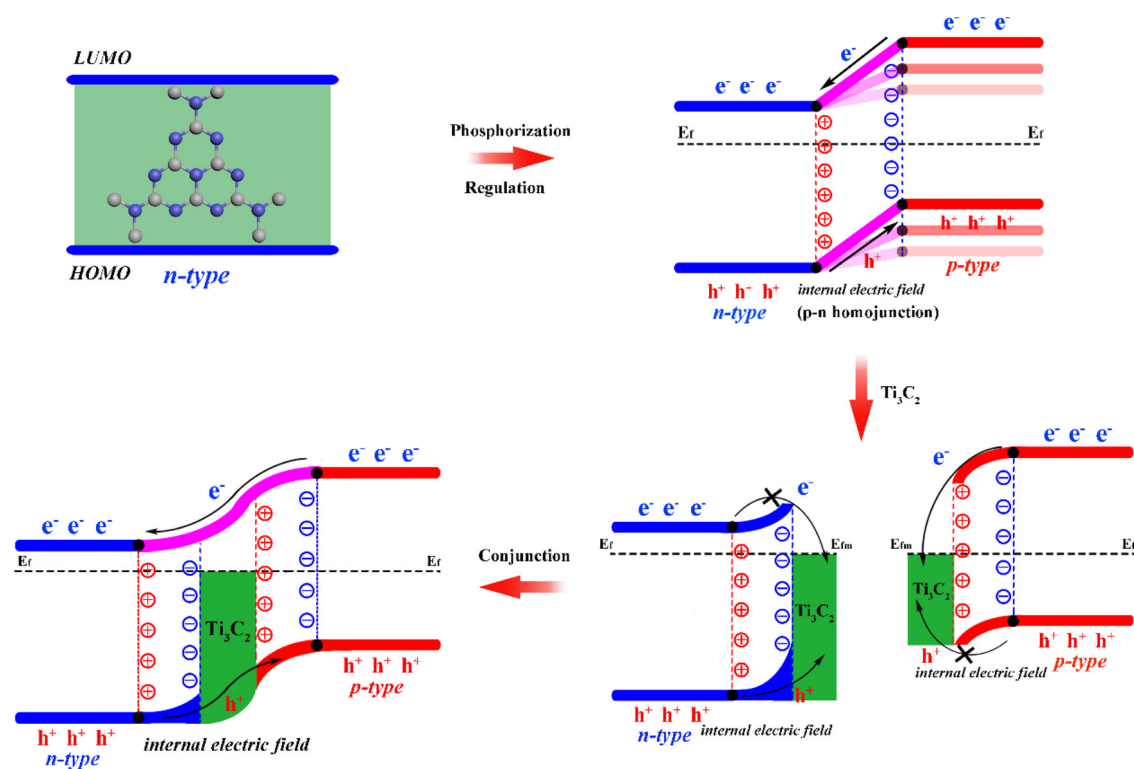
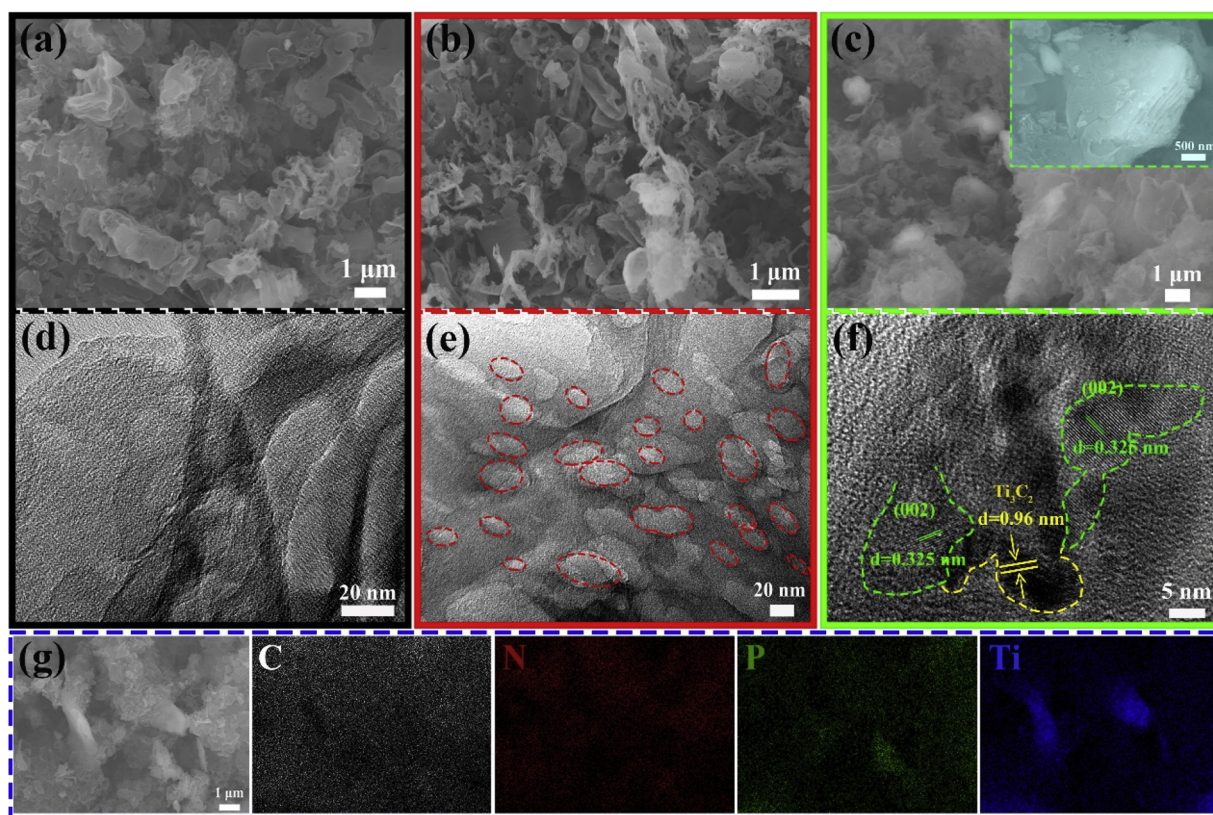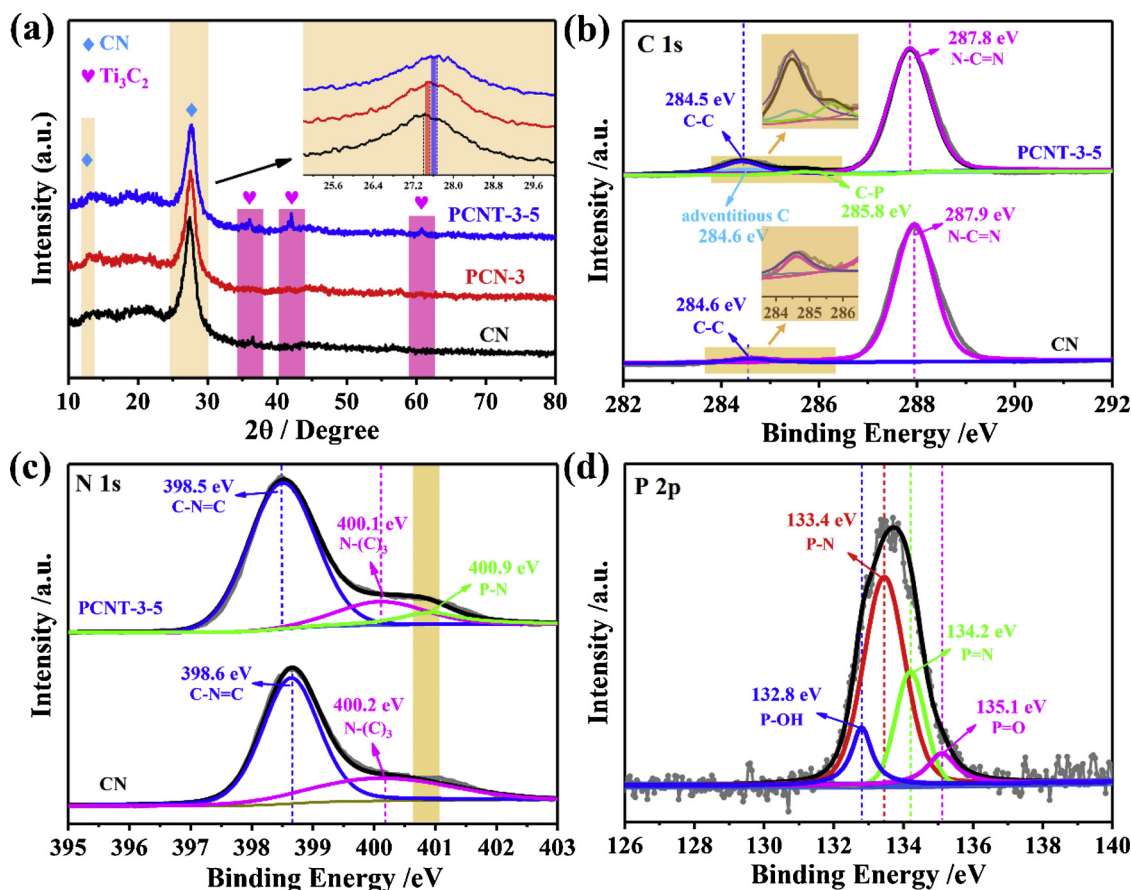**Scheme 1.** Schematic band diagram of P-doped g-C₃N₄/Ti₃C₂ photocatalytic system.

Fig. 1. SEM images of (a) CN, (b) PCN-3, and (c) PCNT-3-5 (inset is the SEM image for PCN-3/Ti₃C₂). TEM images of (d) CN, (e) PCN-3, and (f) PCNT-3-5. (g) The corresponding EDS elemental mapping images of C, N, P and Ti elements in PCNT-3-5.

Fig. 2. (a) XRD patterns of raw CN, PCN-3 and PCNT-3-5 samples. The high resolution XPS spectra of (b) C 1s and (c) N 1s in pure CN and PCNT-3-5. (d) The high resolution XPS spectrum of P 2p in PCNT-3-5.

based) building blocks are confirmed by some peaks from 800 to 900 cm^{-1} [46]. The broad modes at 3100-3300 cm^{-1} come from the stretching vibration of N−H or OH− bond. After doping P element, the peak at 811 cm^{-1} from the bending vibration of heptazine rings becomes weak. It is noteworthy that the vibration band from P-related functional groups can hardly be observed due to the low concentration of P element, apart from the thin peak at 667 cm^{-1} which can be ascribed to the stretching mode of P−N [47] (Fig. S13, inset). The preserved π-delocalized electronic system of CN ensures that the photogenerated charges can transfer to active sites rapidly. As can be seen in Raman spectra (Fig. S14), comparing with CN, the typical D, G bands of PCN-3 exhibit a right shift, also implying the successful doping of P element. X-ray photoelectron spectra (XPS) were conducted to further reveal the electronic structure and chemical compositions of CN and PCNT-3-5. As depicted in Fig. S15, the full XPS spectrum of PCNT-3-5 shows the C 1s, N 1s, Ti 2p and P 2p. The high-resolution XPS spectrum of C 1s (Fig. 2b) possesses two main peaks at around 284.5 and 287.8 eV. They originate from the C−C bonds and sp^2-hybridized carbon in an N-containing aromatic ring (N−CN≡), respectively. In addition, the peak at around 284.6 eV belongs to the adventitious C. Whereas, an extra peak at 285.8 eV of PCNT-3-5 can be observed due to the formation of new C–P bond. The analogous phenomenon can also be noticed in N 1s spectrum (Fig. 2c). Two main peaks at 398.5 and 400.1 eV correspond to the sp^2-hybridized nitrogen in C-containing triazine rings (C−NC≡) and tertiary nitrogen (N-(C)$_3$), respectively. And there is a new peak at 400.9 eV from P−N bond in PCNT-3-5. The spectrum of P 2p (Fig. 2d) can be divided into four peaks, including the peak at 132.8 eV from P−OH bond and the peak at 135.1 eV from P═O bond because of partial oxidation effect [48]. Additional two peaks at 133.4 and 134.2 eV stemming from P−N and PN≡ bonds suggest the

replacement of C atoms by P atoms in CN. Besides, the electronegativity of N element is stronger than P element, suggesting that the P element is easy to lose electrons and possesses typical electron donating character. Thus, the positive valence state of P element induces that the main species of charge carriers are the holes, endowing itself with a p-type feature. Besides, the high-resolution XPS spectrum of Ti 2p displays four peaks (Fig. S16), corresponding to Ti-O and Ti-C bonds. Combining with above analyses, PCNT-3-5 is fabricated successfully by an inverse phosphatizing regulation way.

The overall water splitting performances of as-obtained samples were evaluated in pure water without any sacrificial reagents under visible light irradiation (λ ≥ 420 nm). The comparison of the gas evolution in 5 h is shown in Fig. 3a. The pristine CN has no O$_2$ evolution but an inappreciable evolution of H$_2$ (24.5 μmol g^{-1}) because of the fast recombination of photogenerated electrons and holes. Notably, PCN-3 shows an improved gas evolution of H$_2$ (519.4 μmol g^{-1}) and O$_2$ (232.2 μmol g^{-1}) simultaneously, which indicates that the doping of P element indeed prolongs the lifetime of photocarriers. Remarkably, PCNT-3-5 exhibits an incredible high H$_2$ (3135.5 μmol g^{-1}) and O$_2$ (1527.3 μmol g^{-1}) evolution due to the introduction of Ti$_3$C$_2$ which further enhances the separation efficiency of photocarriers. In Fig. 3b, The H$_2$ and O$_2$ evolution rates match well with the molar ratio of constant 2:1 and the rising tendency is obvious. The photocatalytic rate of H$_2$ evolution is improved about 21.2 and 128.2 times. More importantly, the evolution of O$_2$ grows from nothing and is realized with high yield. In addition, the photocatalytic production activity comparison in water splitting at different phosphatizing temperatures was studied in Fig. S17. Among them, PCN-3 displays the optimal performance which can be further regulated through tuning the loading amounts of Ti$_3$C$_2$ (Fig. S18). The photocatalytic H$_2$ production activity
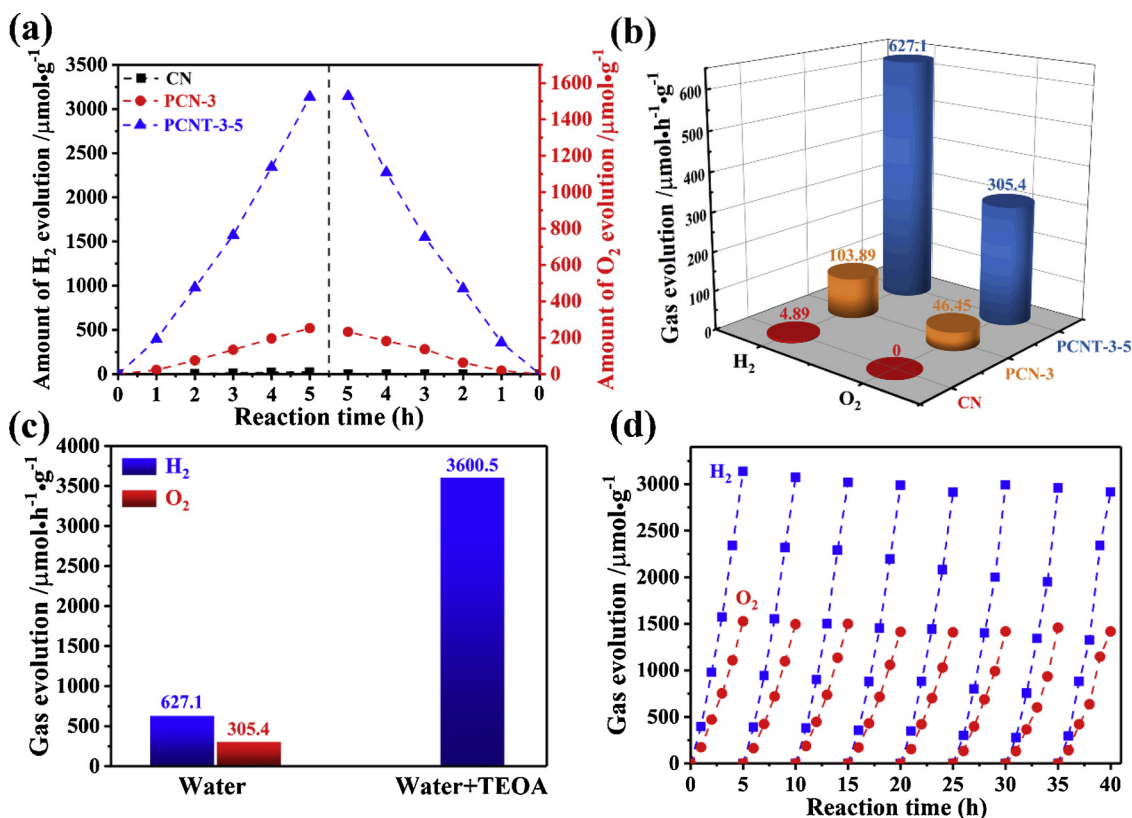
Fig. 3. (a) Comparison of photocatalytic activity of the gas evolution in five hours on CN, PCN-3 and PCNT-3-5. (b) Photocatalytic H_2 and O_2 evolution rates of pristine CN, PCN-3 and PCNT-3-5. (c) The gas evolution rate of PCNT-3-5 in pure water or TEOA. (d) Typical time course of H_2 and O_2 evolution for PCNT-3-5.

with the sacrificial agent (TEOA) was conducted as shown in Fig. 3c, which shows that PCNT-3-5 exhibits a high photocatalytic activity of $3600.5 \,\mu\text{mol h}^{-1\,\text{g}^{-1}}$. This result proves that the lifetime of photo-generated electrons can be enhanced again with the help of TEOA, indicating the potential of PCNT-3-5 in photocatalytic degradation. What's more, PCNT-3-5 has superior photocatalytic water splitting ability than all reported CN-based photocatalysts so far (Table S2). The photocatalytic stability and practicability were evaluated by the re-cycling experiment under artificial solar light. The simultaneous H_2 and O_2 evolution can be observed with unnoticeable trend of decline after 40 h loops (Fig. 3d). The phenomenon of slightly decrease in performance may be attributed to inevitable quality loss of photocatalysts during the recycling process. The high stability is ascribed to its distinct tough structure and has great application potential in overall water splitting.

To make a clear comprehension about the eminent photocatalytic performance, it's essential to extend the light absorption region for improving the solar light utilization and producing more photo-generated electron-hole pairs. What's more, the color of CN changes from white to pale yellow after being doped by P element and becomes light black through further integrating with suitable amount of Ti_3C_2, implying the ameliorative optical property and light harvesting ability (Fig. 4a, inset). Thus, the optical properties of as-obtained samples were studied via the UV–vis absorption spectra as shown in Fig. 4a. The raw CN displays weak absorption intensity, the major absorbing region of which focuses in ultraviolet range ($\lambda < 440 \,\text{nm}$). After phosphating treatment, PCN-3 presents an enhanced feature of absorbance intensity, especially in the range from 440 to 600 nm. Besides, the semblable phenomenon can be observed with different phosphatizing temperatures (Fig. S19). Furthermore, the absorption range of PCNT-3-5 is ef-fectively broaden to the whole visible light region ($\lambda < 800 \,\text{nm}$) which occupies about 52% of all range of sunlight. Similar trend also can be proved again in other proportions of Ti_3C_2 (Fig. S20). The superior

sunlight capture ability mainly comes from the adjustment of band gap under the regulation of P element and Ti_3C_2, which paves the way for the next photon excitation procedure. The insight of generation and separation of photogenerated electron-hole pairs is precondition for the following redox reaction. The time-resolved photoluminescence (TRPL) decay spectra of samples are exhibited as a function of time (Fig. 4b). The average lifetime can be calculated via a quadratic exponential function fitting and the results are listed in Table S3. Among these average lifetimes, CN shows the shortest lifetime of 3.51 ns. In contrast, PCN-3 and PCNT-3-5 exhibit longer lifetime of 4.87 and 5.36 ns, re-spectively. The result can be ascribed to the improved separation and transfer efficiency of photocarriers deriving from the regulation of en-ergy band structure. As shown in the inset of Fig. 4b, the steady-state photoluminescence (PL) spectra were employed to study the re-combination efficiency of photogenerated electron-hole pairs. Ob-viously, CN exhibits the highest emission peak at around 450 nm, in-dicating that the photogenerated electrons and holes will recombine quickly due to the limitation of structure. But the emission peak of PCN-3 is much weaker than CN and shows a slight redshift feature because of the alteration in intrinsic electronic band structure. This also confirms that the doped P element has affected the semiconducting nature of CN, which effectively reduces the recombination probability of photo-generated electrons and holes. The PL emission intensity of PCNT-3-5 is much more remarkably decreased, meaning the introduction of Ti_3C_2 connects PCN-3 nanosheets with each other to shorten the diffusion distance of charges migration and provides lots of surface terminal sites to realize the re-localization of electrons. What's more, the transient photocurrent (TPC) measurement was also carried out to investigate the photo-responsive activity and separation efficiency of photo-induced charges (Fig. S21). PCN-3 presents a better photocurrent intensity than CN. And PCNT-3-5 possesses the highest photocurrent and stable be-havior under intermittent light irradiation, which reveals that the se-paration and migration of photogenerated carriers are boosted
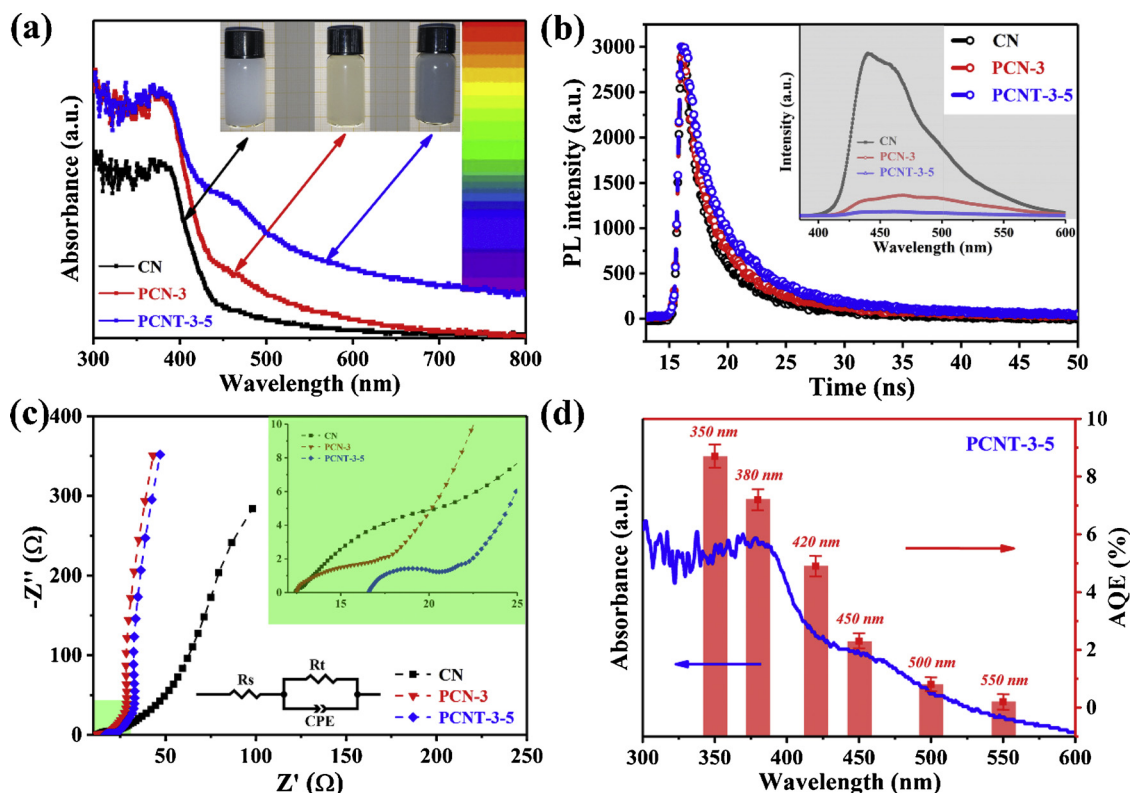
Fig. 4. (a) UV–vis absorption spectra of CN, PCN-3 and PCNT-3-5, inset: The photographs of CN, PCN-3 and PCNT-3-5 solution. (b) Fluorescent lifetime spectra of CN, PCN-3 and PCNT-3-5, inset: Room temperature (298 K) steady-state PL spectra of CN, PCN-3 and PCNT-3-5. (c) Electrochemical impedance spectra (EIS) of CN, PCN-3 and PCNT-3-5, inset: An equivalent circuit impedance diagram. (d) Wavelength-dependent AQE of water splitting over PCNT-3-5 (red dots)), and UV–vis absorption spectrum of PCNT-3-5 (blue) (For interpretation of the references to colour in this figure legend, the reader is referred to the web version of this article).

effectually. The electrochemical impedance spectroscopy (EIS) was used to understand the transfer efficiency of photocarriers at the electrodes. Fig. 4c exposes the EIS Nyquist curves of the samples, which can be simulated well via an electrical equivalent circuit (Fig. 4c, inset). The electrolyte resistance and the interfacial charge-transfer resistance can be represented by R_s and R_t. In comparison to PCN-3 and CN, PCNT-3-5 shows the smallest diameter of semicircle, indicating the lowest impedance of interfacial charge transfer between reactant molecules and active sites. The apparent quantum efficiency (AQE) for overall water splitting of PCNT-3-5 was measured under different monochromatic light irradiations (Fig. 4d). The calculated AQE value reaches up to 8.7% at 350 nm and decreases while increasing the irradiation wavelength. The changing trend of AQE value is coincided well with the absorption spectrum, implying the redox reaction is deployed through appropriate light absorption.

On the basis of the above researches, it is vital to understand the relationship between photocatalytic mechanism and performance in depth. Therefore, to gain high separation and transport efficiency of photogenerated charges the electronic band structure regulation of CN needs to be further investigated. According to the Kubelk-Munk equation: $(\alpha h\nu)^\gamma$ versus $h\nu$ from UV–vis spectra (α, h, and ν are the absorption coefficient, Planck constant, and light frequency, and γ is 2 for CN with a direct band gap [49]), the calculated energy bandgaps (E_g) of samples are shown in Fig. 5a. The E_g of CN is estimated to be 2.61 eV. After phosphating treatment, the E_g value of PCN-X (X = 1, 2, 3 and 4) is changed to 2.57, 2.49, 2.43 and 2.41 eV, which tends to decrease with the increase content of P element (Fig. 5a, inset). This phenomenon indicates that the improved absorbability of sunlight paves the way for the generation of photogenerated electrons and holes. However, the simple E_g change is insufficient to explain the excellent activity of overall water splitting. For this reason, the semiconductor types of CN were investigated under different doping content of P

element via the Mott-Schottky plot. It can be observed that CN shows an obvious characteristic of n-type semiconductor (Fig. S22). Surprisingly, the new feature of p-type semiconductor begins to appear with the increasing degree of phosphatization (Fig. 5b). The tendency of transition between n-type and p-type of PCN is becoming increasingly clear. The result shows that the trait of n-type tends to be weak and the character of p-type is becoming more apparent while increasing the doping content of P element. This means P atoms enter CN's crystal lattice and replace the original atoms, which results in the decrease of surface energy due to the larger radius of P atoms and further influences the energy level distribution [50–52]. Thus, the local species of charge carriers are dominated by the holes. In addition, the positions of conduction band (CB) and valence band (VB) have a vital role in ensuring the sufficient potential of overall water splitting. Hence the Mott-Schottky plots of PCN-X were applied to compute the potentials of the CB edges (E_{CB}) by the x-intercepts in the MS plots. With the conversion formula: $E_{(NHE)} = E_{Ag/AgCl} + 0.059 \cdot PH + 0.197$ (PH = 0), the E_{CB} value of CN was calculated to be -0.68 V vs. Ag/AgCl (-0.48 V vs. NHE) (Fig. S23). Moreover, the E_{CB} values of PCN-X (X = 1, 2, 3 and 4) were calculated to be -0.71, -0.74, -0.82 and -0.93 V vs. Ag/AgCl (-0.51, -0.54, -0.62 and -0.73 V vs. NHE) (Fig. S24). The corresponding E_{VB} values are in accordance with bandgap of samples in turn (Fig. 5a). In addition, the VB-XPS analysis (Fig. S25) also shows that the positions of E_{vb} are consistent with these values in Fig. 5c.

Based on the above analysis, the electronic band structures of PCN-X are shown in Fig. 5c. The CN sample possesses the lowest positions of E_{CB} and E_{VB} with the widest bandgap of n-type feature. As the doping content of P element increases, the positions of E_{CB} and E_{VB} become more negative with decreased bandgap. This trend is attributed to the forming of p-type feature in PCN-X. However, the totally transformation from n-type to p-type of CN can't be achieved due to the limitation of doping level of P element, which just guarantees the co-existence of
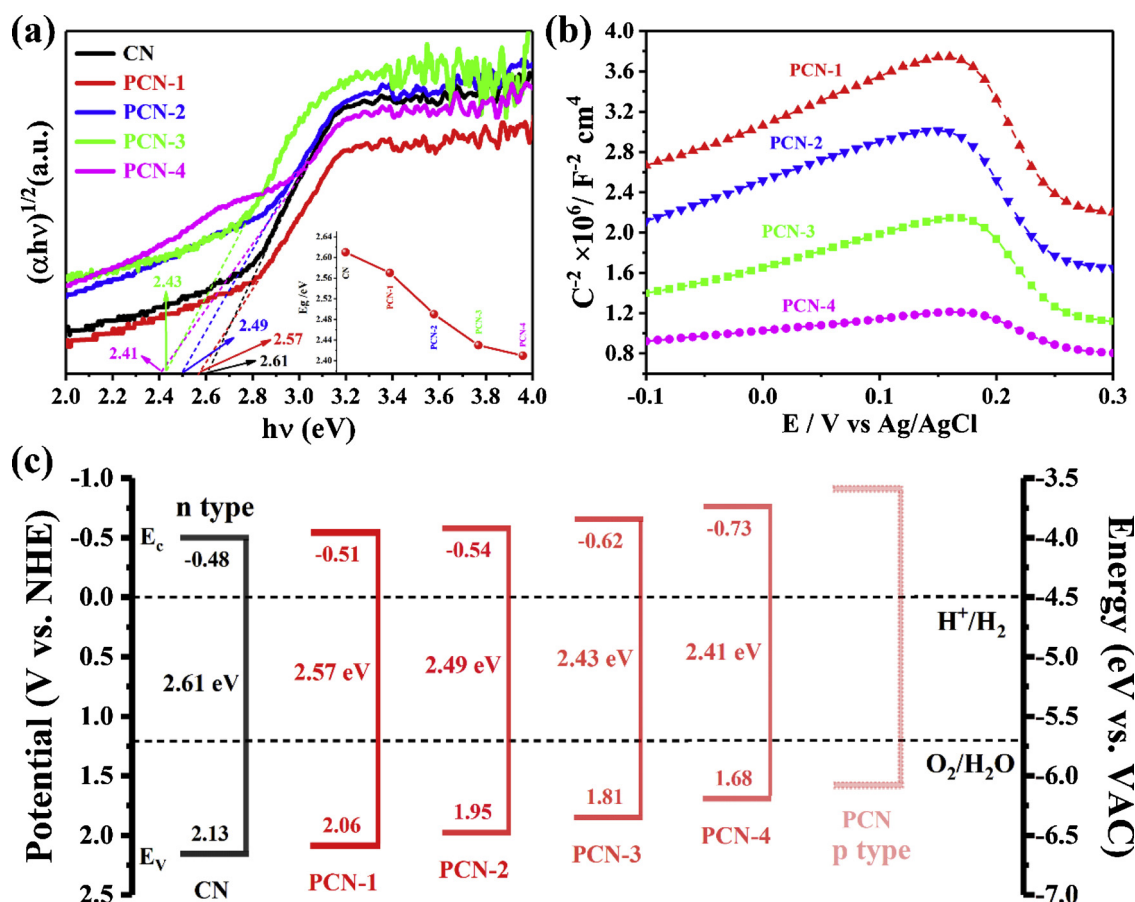
Fig. 5. (a) $(\alpha h\nu)^2$ versus $h\nu$ curves of CN and PCN-X (X = 1, 2, 3 and 4). (b) Mott-Schottky plots of PCN-X (X = 1, 2, 3 and 4). (c) The electronic band structure diagram of CN and PCN-X (X = 1, 2, 3 and 4).

n-type and p-type in PCN-X. Ultimately, a novel p-n homojunction has been generated successfully for the first time via regulating the doping level of P element. By means of the photocatalytic activity comparison in water splitting (Fig. S17), a suitable p-n homojunction can be established in PCN-3. The corresponding schematic energy level mechanism of p-n homojunction is shown in Fig. S26. Compared with p-n heterojunction, p-n homojunction is formed in same material, which is distributed evenly with the robust integration as well as avoids the repellency and compatibility problem of different materials. As a special type of type II junction [53–56], the strong internal electric field is gradually built up at the interface due to the concentration difference in electrons and holes, which leads to the charge redistribution and forms a powerful unidirectional electric field. At the same time, the n-type part with low work function (high E_f) loses electrons and the p-type part with high work function (low E_f) gives holes, which makes the E_f level achieve a new equilibrium. Therefore, the internal electric field will drive the photogenerated electrons (p-type part) to transfer towards n-type part (high E_f) with the low CB edge and the photogenerated holes (n-type part) towards p-type part (low E_f) with the high VB edge. Meanwhile, the recombination of charges can be inhibited effectively owing to the unidirectional feature of internal electric field. As the main driving force, the internal electric field realizes the first step of prolonging the lifetime of separated electrons and holes. In addition, as an excellent conductor with unique layered structure, Ti_3C_2 was introduced into PNC-3 to construct PCNT-3-5, in which Ti_3C_2 interacted well with n-type and p-type part. This effect will offer the second driving force to further prolong the lifetime of photogenerated electrons and holes, the mechanism diagram of which is depicted in Fig. S27. A little internal electric field will come into being when Ti_3C_2 contacts with the n-type part of PCN-3, the direction of which points to Ti_3C_2.

This facilitates photogenerated holes move to Ti_3C_2 as well as prevents the transfer of electrons. On the contrary, the direction of internal electric field will point to itself when the p-type part of PCN-3 contacts with Ti_3C_2, which promotes the transfer of photogenerated electrons to Ti_3C_2 as well as prevents the migration of holes. Combining with above analyses, the photogenerated electrons and holes can be further separated orderly via Ti_3C_2. Besides, the specific layered structure of Ti_3C_2 can efficiently insulate the photogenerated electrons from holes during the migration process, reducing the probability of recombination. Thus, with the help of triple-internal electric field in p-n homojunction decorated with Ti_3C_2, the lifetime of photogenerated electrons and holes is improved greatly. Ultimately, the separated electrons and holes take part in HER and OER, respectively (Fig. S28). Moreover, the robust structure of PCNT-3-5 is also confirmed by the contrast of XRD patterns before and after stability test (Fig. S29). Incorporating the above results, this novel tunable p-n homojunction compound photocatalyst holds tremendous promise for visible light-driven overall water splitting.

4. Conclusion

In summary, we designed and prepared an original PCN with tunable p-n homojunction by integrating the energy band engineering theory into design concept. The triple-internal electric field is established systematically via further incorporating with Ti_3C_2, significantly improving the separation efficiency and transfer ability of the photo-induced electron-hole pairs for highly overall water splitting. A superior high photocatalytic H_2 and O_2 evolution rates of 627.1 and 305.4 µmol h^{-1}g^{-1} has been achieved simultaneously with an apparent quantum yield of 4.9% at 420 nm. This work paves a new avenue to

design other photocatalytic system with tunable p-n homojunction for sufficient solar energy capture and conversion.

5. Experimental section

5.1. Materials

Titanium, aluminum and graphite were purchased from Aladdin. Hydrofluoric acid (HF) and urea (H_2NCONH_2), sodium hypophosphite ($NaH_2PO_2 \cdot H_2O$), triethanolamine ($C_6H_{15}NO_3$), hydrochloric acid (HCl) and absolute ethanol provided by Sinopharm Chemical Reagent Co. Ltd. (Shanghai) were of analytical reagent grade. All materials were used as received without further purification. Solutions were prepared freshly with deionised water.

5.2. Preparation of g-C_3N_4 (CN) and Ti_3C_2

The pristine CN was prepared by a thermal polymerization method. Firstly, 100 g of urea powders was dissolved into 150 mL of water under stirring. Then, the solution pH was adjusted to 3–4 via HCl (0.5 M). The solution was dried at 80 °C for 24 h and transferred to a round crucible. Secondly, the round crucible was put into a muffle furnace and heated to 550 °C for 2 h with a heating rate of 10 °C min^{-1}. Finally, the CN sample was obtained at room temperature.

Ti, Al and graphite powders were mixed with a molar proportion of 3:1.5:2. Then, the mixture was ball-milled for 2 h and pressed into discs. Under the flowing of Ar gas, the discs were heated to 1200 °C for 2 h in a tube furnace at a rate of 10 °C min^{-1}. The discs were taken out at room temperature and ground into powders. Ti_3C_2 was obtained through immersing Ti_3AlC_2 in 40% HF at room temperature for 48 h. In this process the Al species were selectively removed by HF etching and OH-, O- or F- replaced Al as the terminal groups. The as-prepared sample was filtered, washed with deionized water several times and dried at 80 °C for 24 h in a vacuum drying chamber.

5.3. Preparation of phosphorus doped g-C_3N_4 (PCN)

0.1 g CN was dispersed in 10 mL anhydrous ethanol under stirring. Then, the solution was exposed to ultrasound treatment for 15 min and poured into a little long porcelain boat to dry naturally. 5 g NaH_2PO_2 solid was ground in a mortar and spread on the big porcelain boat. Subsequently, the little long porcelain boat was inverted onto the big porcelain boat. Under the flowing of Ar gas, the samples were heated to 300, 350, 400 and 450 °C (PCN-1, PCN-2, PCN-3 and PCN-4) for 5 h in a tube furnace at a rate of 2 °C min^{-1}. After cooling down to room temperature, PCN samples were obtained.

5.4. Preparation of phosphorus doped g-C_3N_4/Ti_3C_2

0.1 g PCN-3 was dispersed in 10 mL anhydrous ethanol under stirring. An amount of Ti_3C_2 was added into the above solution while keeping the mass percent concentration of Ti_3C_2 in the PCN-3 sample equal to 0%, 1%, 5%, 7%, 10%. The samples were labeled as PCNT-3-Y (Y = 0, 1, 5, 7, 10). Then, the solutions were ultrasound treated for 30 min and poured into a little long porcelain boat to dry naturally. And the samples were maintained at 500 °C for 3 h with a heating rate of 3 °C min^{-1} in a flowing Ar atmosphere. The ultimate g-C_3N_4/Ti_3C_2 products were obtained after cooling to room temperature. Besides, a mechanical grinding experiment of PCN-3 and Ti_3C_2 (5%) was conducted under the same conditions.

5.5. Characterisations

Powder X-ray diffraction (XRD) patterns were recorded on a Bruker D8-Advance X-ray powder diffractometer with a Cu-Kα radiation (λ = 0.15418 nm). Scanning electron microscopy (SEM) images were collected using a Hitachi S-4800 microscope equipped with an energy-dispersive X-ray analyser (EDS, Horiba EMAX Energy EX-350). Transmission electron microscope (TEM) and high resolution transmission electron microscope (HRTEM) images were obtained with a Philips Tecnai 20U-Twin microscope at an acceleration voltage of 200 kV. UV–vis diffuse reflectance spectroscopy (DRS) was conducted using a Shimadzu UV2550 recording spectrophotometer equipped with an integrating sphere with wavelength of 200 to 900 nm. $BaSO_4$ was used as a reference. The room-temperature Raman spectra of samples were recorded on a LabRam HR system from Horiba Jobin Yvon at room temperature using the 532 nm solid laser as the exciting source. X-ray photoelectron spectroscopy (XPS, Thermo ESCALAB 250) was performed using monochromated Al-Kα radiation (1486.8 eV). The photoluminescence (PL) experiment was conducted on a Hitachi F-2700 spectrophotometer using an excitation wavelength of 380 nm. The fluorescent lifetime was obtained by Opolette 355 II Instrument (USA).

5.6. Photocatalytic activity test

Photocatalytic reactions were carried out in a Pyrex reaction cell connected to a closed gas circulation and evacuation system. Ten milligrams of catalysts were dispersed in 100 mL of pure water, while 3 wt % Pt was photo-deposited from H_2PtCl_6 aqueous solution as co-catalyst. Furthermore, ten milligrams of PCNT-3-5 was dispersed in 100 mL of aqueous solution containing 10 mL of triethanolamine as sacrificial agents. The suspension was then thoroughly degassed and irradiated by a Xe lamp (300 W) equipped with an optical cutoff filter (λ = 420 nm) to eliminate ultraviolet light. The temperature of the reactant solution was maintained at 6 °C during the reaction. The amount of H_2 and O_2 produced from water-splitting was analysed using online gas chromatography (Gc7900 Tianmei Shanghai China). The photocatalytic activity was assessed by the average rate of H_2 and O_2 evolution in 5 h. Every five hours, the suspension is thoroughly degassed and retested again. This process is repeated eight more times.

5.7. Photoelectrochemical activity measurements

The PEC measurement system in this study was a CHI660D workstation (Shanghai Chenhua, China) with a three-electrode configuration using the as-obtained samples as the working electrodes, a Pt plate as the counter electrode, Ag/AgCl as the reference electrode. H_2SO_4 aqueous solution (0.5 M) was used as the electrolyte. The working electrodes were prepared as follows: 10 mg of as-prepared samples were dispersed in absolute ethanol and the suspension was directly deposited onto an FTO conductive glass plate and then dried at 80 °C in a vacuum oven.

Declaration of Competing Interest

The authors declare that they have no known competing financial interests or personal relationships that could have appeared to influence the work reported in this paper.

Appendix A. Supplementary data

Supplementary material related to this article can be found, in the online version, at doi:https://doi.org/10.1016/j.apcatb.2019.118077.

References

[1] X. Wang, K. Maeda, A. Thomas, K. Takanabe, G. Xin, J.M. Carlsson, K. Domen, M. Antonietti, Nat. Mater. 8 (2009) 76–80.
[2] G.W. Crabtree, N.S. Lewis, Phys. Today 60 (2007) 37–42.
[3] A.J. Nozik, Ann. Rev. Phys. Chem. 29 (1978) 189–222.
[4] Y. Kageshima, T. Shinagawa, T. Kuwata, J. Nakata, T. Minegishi, K. Takanabe, K. Domen, Sci. Rep. 6 (2016) 24633.
[5] H. Tada, T. Mitsui, T. Kiyonaga, T. Akita, K. Tanaka, Nat. Mater. 5 (2006) 782–786.
[6] A. Iwase, Y.H. Ng, Y. Ishiguro, A. Kudo, R. Amal, J. Am. Chem. Soc. 133 (2011) 11054–11057.
[7] H. Kato, M. Hori, R. Konta, Y. Shimodaira, A. Kudo, Chem. Lett. 33 (2004) 1348–1349.
[8] G. Ananyev, G.C. Dismukes, Photosynth. Res. 84 (2005) 355–365.
[9] F. Cheng, J. Shen, B. Peng, Y. Pan, Z. Tao, J. Chen, Nat. Chem. 3 (2011) 79–84.
[10] G. Zhang, Z.-A. Lan, X. Wang, Chem. Sci. 8 (2017) 5261–5274.
[11] Y. An, Y. Liu, P. An, J. Dong, B. Xu, Y. Dai, X. Qin, X. Zhang, M.-H. Whangbo, B. Huang, Angew. Chem. Int. Ed. 56 (2017) 3036–3040.
[12] J. Yan, H. Wu, H. Chen, Y. Zhang, F. Zhang, S.F. Liu, Appl. Catal. B 191 (2016) 130–137.
[13] M.G. Kibria, R. Qiao, W. Yang, I. Boukahil, X. Kong, F.A. Chowdhury, M.L. Trudeau, W. Ji, H. Guo, F.J. Himpsel, L. Vayssieres, Z. Mi, Adv. Mater. 28 (2016) 8388–8397.
[14] W. Che, W. Cheng, T. Yao, F. Tang, W. Liu, H. Su, Y. Huang, Q. Liu, J. Liu, F. Hu, Z. Pan, Z. Sun, S. Wei, J. Am. Chem. Soc. 139 (2017) 3021–3026.
[15] J. Zhang, J. Sun, K. Maeda, K. Domen, P. Liu, M. Antonietti, X. Fu, X. Wang, Energy Environ. Sci. 4 (2011) 675–678.
[16] H. Wang, Y. Su, H. Zhao, H. Yu, S. Chen, Y. Zhang, X. Quan, Environ. Sci. Technol. 48 (2014) 11984–11990.
[17] Y. Li, R. Jin, Y. Xing, J. Li, S. Song, X. Liu, M. Li, R. Jin, Adv. Energy Mater. 6 (2016) 1601273.
[18] J. Liu, Y. Liu, N. Liu, Y. Han, X. Zhang, H. Huang, Y. Lifshitz, S.-T. Lee, J. Zhong, Z. Kang, Science 347 (2015) 970–974.
[19] G. Dong, K. Zhao, L. Zhang, Chem. Commun. 48 (2012) 6178–6180.
[20] Y. Yu, J. Geng, H. Li, R. Bao, H. Chen, W. Wang, J. Xia, W.-Y. Wong, Sol. Energy Mater. Sol. Cells 168 (2017) 91–99.
[21] F. Dong, Z. Zhao, T. Xiong, Z. Ni, W. Zhang, Y. Sun, W.-K. Ho, ACS Appl. Mater. Interfaces 5 (2013) 11392–11401.
[22] F. Guo, W. Shi, C. Zhu, H. Li, Z. Kang, Appl. Catal. B 226 (2018) 412–420.
[23] Y. Li, Y. Xue, J. Tian, X. Song, X. Zhang, X. Wang, H. Cui, Sol. Energy Mater. Sol. Cells 168 (2017) 100–111.
[24] Y. Zhou, L. Zhang, J. Liu, X. Fan, B. Wang, M. Wang, W. Ren, J. Wang, M. Li, J. Shi, J. Mater. Chem. A 3 (2015) 3862–3867.
[25] J. Ran, T.Y. Ma, G. Gao, X.-W. Du, S.Z. Qiao, Energy Environ. Sci. 8 (2015) 3708–3717.
[26] L. Yang, S. Luo, Y. Li, Y. Xiao, Q. Kang, Q. Cai, Environ. Sci. Technol. 44 (2010) 7641–7646.
[27] H. Wang, L. Zhang, Z. Chen, J. Hu, S. Li, Z. Wang, J. Liu, X. Wang, Chem. Soc. Rev. 43 (2014) 5234–5244.
[28] Y. Ao, K. Wang, P. Wang, C. Wang, J. Hou, Appl. Catal. B 194 (2016) 157–168.
[29] T. Jiang, T. Xie, W. Yang, L. Chen, H. Fan, D. Wang, J. Phys. Chem. C 117 (2013) 4619–4624.
[30] S. Nakamura, T. Mukai, M. Senoh, J. Appl. Phys. 30 (1991) L1998–L2001.
[31] M.-T. Chen, M.-P. Lu, Y.-J. Wu, J. Song, C.-Y. Lee, M.-Y. Lu, Y.-C. Chang, L.-J. Chou, Z.L. Wang, L.-J. Chen, Nano Lett. 10 (2010) 4387–4393.
[32] L. Pan, S. Wang, J. Xie, L. Wang, X. Zhang, J.-J. Zou, Nano Energy 28 (2016) 296–303.
[33] X. Wang, Q. Xu, M. Li, S. Shen, X. Wang, Y. Wang, Z. Feng, J. Shi, H. Han, C. Li, Angew. Chem. Int. Ed. 51 (2012) 13089.
[34] G. Liu, G. Zhao, W. Zhou, Y. Liu, H. Pang, H. Zhang, D. Hao, X. Meng, P. Li, T. Kako, J. Ye, Adv. Funct. Mater. 26 (2016) 6822–6829.
[35] M.R. Lukatskaya, O. Mashtalir, C.E. Ren, Y. Dall'Agnese, P. Rozier, P.L. Taberna, M. Naguib, P. Simon, M.W. Barsoum, Y. Gogotsi, Science 341 (2013) 1502–1505.
[36] M. Ghidiu, M.R. Lukatskaya, M.-Q. Zhao, Y. Gogotsi, M.W. Barsoum, Nature 516 (2014) 78–81.
[37] J. Ran, G. Gao, F.-T. Li, T.-Y. Ma, A. Du, S.-Z. Qiao, Nat. Commun. 8 (2017) 13907.
[38] M. Pandey, K.S. Thygesen, J. Phys. Chem. C 121 (2017) 13593–13598.
[39] T. Cai, L. Wang, Y. Liu, S. Zhang, W. Dong, H. Chen, X. Yi, J. Yuan, X. Xia, C. Liu, S. Luo, Appl. Catal. B 239 (2018) 545–554.
[40] H. Wang, Y. Sun, Y. Wu, W. Tu, S. Wu, X. Yuan, G. Zeng, Z.J. Xu, S. Li, J.W. Chew, Appl. Catal. B 245 (2019) 290–301.
[41] C. Ling, L. Shi, Y. Ouyang, J. Wang, Chem. Mater. 28 (2016) 9026–9032.
[42] S. Li, P. Tuo, J. Xie, X. Zhang, J. Xu, J. Bao, B. Pan, Y. Xie, Nano Energy 47 (2018) 512–518.
[43] J. Xu, L. Zhang, R. Shi, Y. Zhu, J. Mater. Chem. A 1 (2013) 14766.
[44] J. Chen, Z. Hong, Y. Chen, B. Lin, B. Gao, Mater. Lett. 145 (2015) 129–132.
[45] L. Jing, R. Zhu, D.L. Phillips, J.C. Yu, Adv. Funct. Mater. 27 (2017) 1703484.
[46] W.-J. Ong, L.-L. Tan, Y.H. Ng, S.-T. Yong, S.-P. Chai, Chem. Rev. 116 (2016) 7159–7329.
[47] L.S. Hersh, E.C. Onyiriuka, W. Hertl, J. Mater. Res. 10 (1995) 2120–2127.
[48] Y.-P. Zhu, T.-Z. Ren, Z.-Y. Yuan, ACS Appl. Mater. Interfaces 7 (2015) 16850–16856.
[49] W. Zhao, W. Ma, C. Chen, J. Zhao, Z. Shuai, J. Am. Chem. Soc. 126 (2004) 4782–4783.
[50] M.S. Daw, M.I. Baskes, Phys. Rev. B 29 (1984) 6443–6453.
[51] G. Ryschenkow, M. Kleman, J. Chem. Phys. 64 (1976) 404–412.
[52] O. Mondain-Monval, J.C. Dedieu, T. Gulik-Krzywicki, P. Poulin, Eur. Phys. J. B 12 (1999) 167–170.
[53] B. Ma, J. Yang, H. Han, J. Wang, X. Zhang, C. Li, J. Phys. Chem. C 114 (2010) 12818–12822.
[54] D. Sarkar, C.K. Ghosh, S. Mukherjee, K.K. Chattopadhyay, ACS Appl. Mater. Interrfaces 5 (2013) 331–337.
[55] B. Ma, K. Lin, W. Su, W. Liu, Appl. Surf. Sci. 317 (2014) 682–687.
[56] B. Ma, J. Kim, T. Wang, J. Li, K. Lin, W. Liu, S. Woo, RSC Adv. 5 (2015) 79815–79819.